Smart Materials and Structures

PAPER

Development of a magnetorheological-based electrical robotic joint with characteristics of high load capability and high energy efficiency

To cite this article: Erwin Ang Tien Yew *et al* 2026 *Smart Mater. Struct.* **35** 085003

Smart Materials and Structures

Check for updates

RECEIVED
2 February 2026

REVISED
5 June 2026

ACCEPTED FOR PUBLICATION
23 June 2026

PUBLISHED
3 August 2026

PAPER

Development of a magnetorheological-based electrical robotic joint with characteristics of high load capability and high energy efficiency

Erwin Ang Tien Yew[1,2], Wenbo Li[1,2], Xianlong Mai[1,2], Zirui Chen[1,2], Liang Zhang[3,*] and Shuaishuai Sun[1,2,*]

[1] CAS Key Laboratory of Mechanical Behavior and Design of Materials, School of Engineering Sciences, University of Science and Technology of China, Hefei, Anhui 230026, People's Republic of China
[2] Institute of Humanoid Robots, School of Engineering Sciences, University of Science and Technology of China, Hefei, Anhui 230026, People's Republic of China
[3] School of Electrical Engineering and Automation, Anhui University, Hefei, Anhui 230601, People's Republic of China
[*] Authors to whom any correspondence should be addressed.

E-mail: liangzhang@ahu.edu.cn and sssun@ustc.edu.cn

Keywords: magnetorheological robotics joint, magnetorheological actuator, magnetorheological bearing, single-legged robot

Supplementary material for this article is available online

Abstract

With the rapid advancement of robotics in industrial, exploration, logistics, and domestic applications, actuator performance has become a critical factor in enabling robust and energy-efficient operation. While electric actuators offer compactness and precise control, they often suffer from limited load capacity and high energy consumption under sustained loads and impact conditions.To address these challenges, we propose a compact magnetorheological (MR)-enhanced joint that integrates electric actuation with MR damping. The proposed joint enables seamless switching between electric actuation and MR-based damping modes, exploiting the field-dependent rheological properties of magnetorheological fluid to enhance impact mitigation and passive load-holding capability. Experimental characterization shows that the proposed MR actuator achieves a torque-to-mass ratio (TMR) of 174.3 $\mathrm{Nm\,kg^{-1}}$ and a torque-to-volume ratio (TVR) of 4.21×10^{-4} $\mathrm{Nm\,mm^{-3}}$. When evaluated at the joint level, the system exhibits a TMR of 52.3 $\mathrm{Nm\,kg^{-1}}$ and a TVR of 8.4×10^{-5} $\mathrm{Nm\,mm^{-3}}$. On a single-legged robotic testbed, the MR-enhanced joint reduces peak impact torque by 28% and peak vertical acceleration by 11.5% during free-fall landing compared to a purely electric baseline. In addition, quasi-static load tests demonstrate that the joint supports a 9 kg payload while consuming only 8 W, compared to 6 kg at 22.8 W for the baseline configuration. These results demonstrate that the proposed MR-enhanced joint provides improved impact robustness, increased load capacity, and reduced energy consumption within a compact and easily integrable actuator architecture.

1. Introduction

Actuator performance has become increasingly critical with the rapid advancement of robotics, as actuators serve as the primary drivers of locomotion and manipulation in quadruped and humanoid robots. Key performance factors, including Torque-to-Mass Ratio (TMR) and energy efficiency, directly determine the overall capabilities of a robotic system. Among existing actuation technologies, pneumatic and hydraulic actuators can deliver high power density but suffer from bulky auxiliary hardware, limited efficiency, and maintenance complexity, which restrict their practicality in mobile and field robots [1–8]. As a result, electric actuators have become the dominant solution due to their compact form, low weight, and precise controllability [9–11]. In most electric robotic systems, planetary gear transmissions are employed to achieve the torque levels required for legged locomotion within a compact actuator volume. Higher output torque in planetary actuators is commonly achieved through increased gear ratios or enlarged motor stators, leading to increased actuator volume and mass [12]. Moreover, sustained high-load operation and impact events can lead to overheating [13], reduced energy efficiency [14, 15], and, in severe cases, overcurrent protection or shutdown [16]. These limitations motivate the exploration of complementary mechanisms that can enhance the robustness and load-handling capability of compact planetary actuators.

In response to the limitations of purely rigid electric actuators, elastic elements have been widely introduced into robotic actuation architectures to provide mechanical compliance. Elastic actuation can effectively mitigate impact loads and improve force controllability by temporarily storing mechanical energy. However, elastic elements inherently introduce nonlinear dynamics and do not directly provide tunable damping or passive load-holding capability under sustained loads. While elastic actuation improves robustness to impacts, it offers limited benefits for sustained high-load operation or energy-efficient load support, motivating the exploration of alternative approaches that can provide controllable dissipation and resistance within compact actuator structures.

Magnetorheological fluids (MRF) are intelligent materials whose apparent viscosity and yield stress increase rapidly under an applied magnetic field [17]. In robotic systems, these field-dependent properties enable MRF to be employed in different roles depending on the actuation objective. For active robotic actuation, MRF are commonly integrated as MR clutches [18, 19] or Magnetorheological Actuator (MRA) [20, 21] to regulate torque transmission within a drivetrain. In particular, Plante *et al* [22] demonstrated that MR-based clutch actuators can function as a fluidic torque interface that decouples motor inertia from the output, enabling robotic joints to dynamically transition between low mechanical impedance with high backdrivability for haptic interaction and high torque density and stiffness for collaborative robotic tasks. Overall, these results demonstrate that MRA are capable of providing a tunable impedance range, high-force load-bearing, and intrinsic impact mitigation within a unified actuation framework.

In contrast to active actuation paradigms, MRF are also widely employed in a passive or semi-active manner within assistive and rehabilitation systems. In both lower- and upper-limb exoskeletons, MR dampers are commonly integrated at the joint level to facilitate load transfer, dissipate impact energy, and enhance load-carrying capability. In such applications, the MR element primarily functions as a controllable resistive component, rather than as a primary torque source for direct rehabilitation or motion assistance. Representative studies have demonstrated that MR-based exoskeletons can effectively reduce the ground reaction force experienced by users during load-carrying locomotion, and improve human load-bearing capability while alleviating musculoskeletal loading [23, 24].

Building upon these active and passive uses of MRF in robotics, recent research has explored MR-based actuation architectures that integrate controllable impedance directly into robotic joints and transmissions. In most existing designs, MR functionality is realized through dedicated clutch or damper modules that are either externally coupled to the actuation system or implemented as self-contained MR actuator units. While these approaches enable effective torque modulation or energy dissipation, they typically introduce additional mechanical interfaces and transmission stages that are difficult to accommodate within commercial off-the-shelf actuators. As a result, substantial redesign of the drivetrain or joint layout is often required before such MR devices can be deployed in practical robotic systems. These requirements pose particular challenges for compact planetary actuators commonly used in legged robots, where available space and drivetrain simplicity are tightly constrained. The added volume associated with dedicated MR modules can limit retrofit feasibility and complicate integration into existing actuator housings. To address these challenges, we propose a simple and compact MR-enhanced planetary actuator that integrates controllable damping directly into the existing transmission structure. Rather than introducing additional clutch stages or standalone MR modules, the proposed approach replaces conventional planet gears with MR-enabled planet gear units incorporating MR bearings.

Based on this integration-focused design philosophy, the main contributions of this work are summarized as follows:

- A simple and compact method for integrating MR damping into a standard planetary actuator by replacing conventional needle bearings with MR-enabled planet gear units, requiring minimal structural modification.
- A geared-stage MR bearing integration strategy that positions the MR element at a reduced rotational speed, enabling high yield resistive torque generation and effective damping.
- Experimental validation on a robotic joint and a single-leg testbed, demonstrating improved impact mitigation, increased load-holding capability, and reduced electrical power consumption compared to a purely electric baseline.

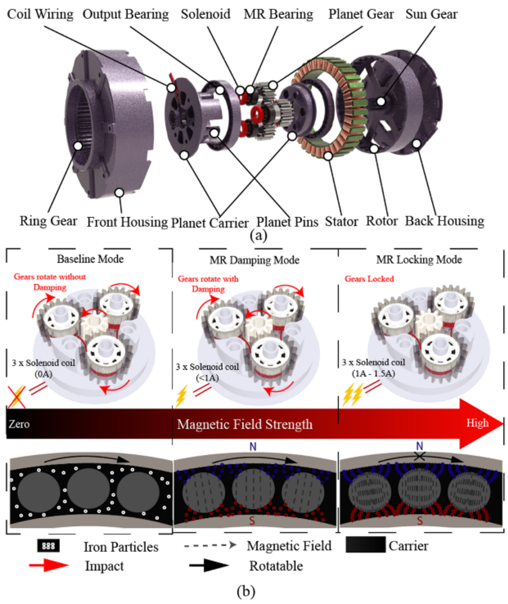

Figure 1. (a) Exploded view of MR-based robotic joint (MR-Joint) (b) working principle of MRA.

The rest of this article is organized as follows. Section 2 introduces the design and working principle of the proposed MRA. Section 3 presents a simplified MR-bearing torque representation and its integration with the actuator-level control framework. Section 4 evaluates the mechanical characteristics of the MRA. Section 5 presents the application of the MRA on a single-legged robot. Section 6 provides discussion, and section 7 concludes the article.

2. System overview

2.1. Design of MR-based robotic joint

A conventional planetary electric actuator consists of two primary subsystems: an electronic subsystem and a mechanical transmission subsystem. The electronic subsystem includes the stator and rotor, which enable precise torque and position control, while the mechanical subsystem typically employs a planetary gear train to amplify output torque within a compact volume.

In the proposed design, the conventional planetary gear system is replaced by a compact MR planetary system, referred to as the MRA. Unlike traditional planetary designs, the MRA integrates MR bearings directly into hollow planetary gears. This configuration allows the MR elements to utilize unused internal volume within the gearbox and ensures that the MRF operates at the reduced rotational speeds of the geared stage, thereby avoiding the high shear rates associated with rotor-side integration.

By positioning the MR elements between the electric motor and the reaction torque path, the MRA is able to effectively attenuate impact loads before they are transmitted to the motor. This placement enables the MR bearings to act as a controllable resistive interface during transient loading events, improving impact robustness without altering the external form factor of the actuator. An exploded view of the proposed MR-Joint is shown in figure 1(a).

Considering the limited radial space available within the planetary gear stage, the MR bearing geometry imposes strict constraints on fluid volume, coil size, and sealing. To preserve sufficient gear tooth thickness for reliable torque transmission, a compact sealed bearing configuration was adopted. The limited available volume further motivated the use of fine copper wire (0.25 mm diameter) with a high turn count (156 turns), enabling adequate magnetic field strength within the confined space.

To ensure an effective MR response within the small active volume, a high-performance MRF formulation was selected. Fine iron particles (1–3 μm) were used to maintain fluidity and reduce friction and wear under rolling contact, while a high particle concentration (87.7 wt.%) was employed to increase the field-induced yield stress and enhance resistance to centrifugal leakage. Collectively, these design choices balance electromagnetic efficiency,

Table 1. Specification of MRA.

Wire Diameter (mm)	0.25
Coil thickness (mm)	3.25
Coil resistance (Ω)	5
Coil inner/Outer diameter (mm)	7/13
Bearing thickness (mm)	5
Bearing inner/Outer diameter (mm)	6.0/15.0
Number of coil turns	156
MRF (wt.%)	87.70%
Mass of MRF (g)	5
Motor mass (g)	526
Motor mass with MRA (g)	590

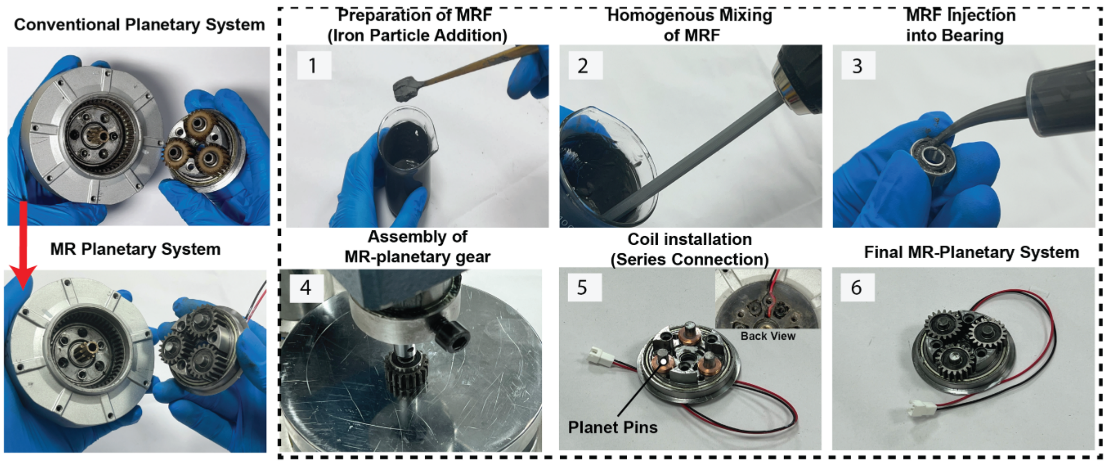

Figure 2. Overview of the MR-enhanced planetary system fabrication, from MRF preparation and bearing injection to coil integration and final assembly.

MR performance, mechanical integrity, and integration feasibility within the planetary gear stage. The main design specifications of the proposed MRA are summarized in table 1.

2.2. Working principle of MRA

The working principle of the proposed MRA is illustrated in figure 1(b). In **Baseline Mode**, the actuator operates under purely electric actuation with no excitation current applied to the MRA ($I = 0$ A). In this state, the MRF remains in a liquid phase, and the MR bearings rotate freely with minimal additional resistive torque.

When the excitation current is applied, the actuator transitions into MR-assisted operating modes that introduce controllable impedance at the joint. In **MR Damping Mode**, the energized MR bearings generate a velocity-dependent resistive torque that acts in parallel with the electric actuator, providing impact attenuation and motion smoothing during dynamic operation. As illustrated in figure 1(b), this mode allows joint motion to continue while dissipating external disturbances through MR-based damping.

Under conditions where MR resistive torque exceeds the applied external load, the actuator operates in **MR Braking Mode**. In this mode, the MR bearing sustains the external load with negligible joint motion, thereby relieving the electric motor from continuous load-bearing and reducing electrical power consumption.

For a given external load, the magnitude of the MR resistive torque is governed by the applied magnetic field strength. Accordingly, adjusting the excitation current enables continuous and reversible modulation between free motion, damped motion, and load-supporting operation.

2.3. MR bearing construction and assembly

The fabrication and assembly procedure of the MRA is illustrated in figure 2. A high particle concentration MRF (87.7 wt.%) was prepared using iron particles with diameters of 1–3 μm. To ensure homogeneous dispersion of the particles, the MRF was heated to 70 °C during preparation. Each sealed bearing

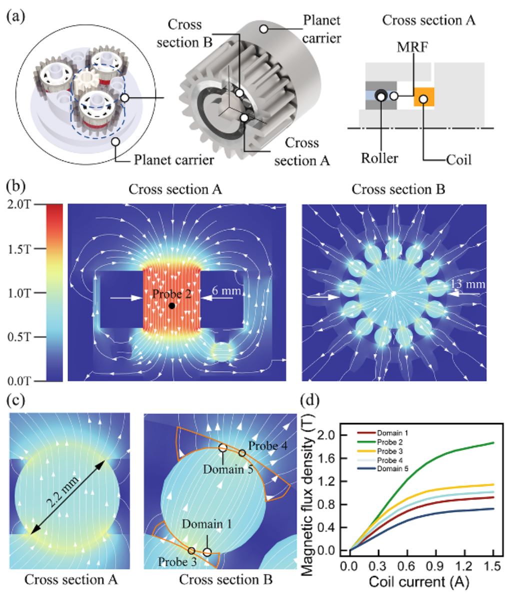

Figure 3. Magnetic simulation results. (a) Preprocessing and model simplification. (b) Vector magnetograms with magnetic flux density. (c) Enlarged view. (d) Magnetic flux density curve corresponding to coil current.

was then filled with approximately 0.1 ml of the prepared MRF.The filled bearing units were vacuum-treated during assembly to reduce trapped air and improve fluid filling before sealing. To suppress fluid leakage during rotation, O-rings were installed between the bearing and its seal.

The MR bearings were interference-fitted onto the planet pins, which are manufactured integrally with the planet carrier, and into the planetary gears using Loctite 638 bearing adhesive, ensuring that the planetary gears rotate directly on the MR bearings. This configuration constrains the mechanism to a single rotational degree of freedom and enables efficient transmission of rotational motion through the MR bearing interface. All electromagnetic coils were electrically connected in series, resulting in a total resistance of approximately 5 Ω. The coil leads were routed outside the planetary carrier to prevent obstruction by the rotating gears.

Plastic washers were placed above the coils to provide both electrical insulation and mechanical isolation between the coils and the rotating bearing components. A clearance of 1 mm was maintained between the coils and the planetary gears to prevent mechanical interference during operation. In addition, a radial clearance of 0.1 mm was maintained between the planetary gears and the planet carrier to minimize friction and ensure smooth rotation. Lubrication was applied to the planetary gears and ring gear to reduce wear and friction and to improve overall transmission efficiency.

2.4. Magnetic field simulation of the MRA

In this work, COMSOL Multiphysics was used as an electromagnetic design tool to guide the design of the MRA by improving magnetic-flux concentration in the active MR bearing region through the dimensional design of the planet carrier and planetary gear. Accordingly, the present study reports the finalized MRA design, together with the corresponding magnetic-field analysis and experimental characterization. A simplified electromagnetic model of the MRA was extracted, as shown in figure 3(a). The model represents one of the three symmetric segments of the planetary system and includes the planet carrier, planetary gear, excitation coil, MR bearing, and MRF.

Material properties were assigned to all components in the simulation. The excitation current supplied to the coil was swept from 0 to 1.5 A with an increment of 0.1 A. The resulting magnetic flux density distribution is shown in figure 3(b). In the enlarged view of the bearing element in cross-section B, magnetic flux lines are observed to concentrate between the rolling element and the bearing raceway. These flux paths guide the ferrous particles in the MRF to form field-aligned particle chains, as highlighted in figure 3(c). This region is responsible for resisting relative motion and transmitting controllable torque. To quantify the magnetic field strength, three point probes and two domain probes were defined around the MR bearing. Probe 3 and Probe 4 were placed in the gaps between the rolling element and the inner and outer bearing rings, respectively. Under a coil current of 1.5 A, the measured magnetic flux densities reached 1.14 T and 1.02 T at these locations. Domain probes located within the

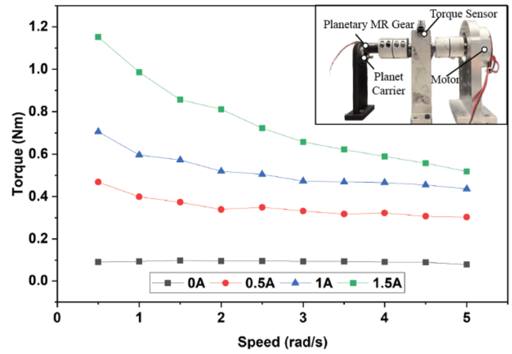

Figure 4. Torque-speed characterization of a single MR bearing at excitation currents of 0, 0.5, 1, and 1.5 A.Inset: experimental setup with planetary MR gear, torque sensor, and motor.

MRF regions recorded flux densities of 0.92 T and 0.72 T. These values confirm that the MR bearing is subjected to a sufficiently strong and controllable magnetic field.

To identify the efficient near-linear operating region of the finalized MRA, Probe 2 was placed near the shaft region of the planet carrier. The results show that, within the current range of 0–0.9 A, the magnetic flux density in the monitored structural region increases approximately linearly with excitation current, as shown in figure 3(d). Therefore, 0–0.9 A defines the efficient operating range for predictable torque modulation of the MRA. At higher currents, the magnetic response gradually departs from linearity. Accordingly, currents up to 1.5 A were retained in the experiments only to characterize the prototype's upper braking-torque capacity. This monotonic increase and subsequent saturation of magnetic flux are consistent with the static torque-current Hill fit introduced in Section III-D which increases with field strength and flattens near magnetic saturation.

3. MR bearing torque representation and control integration

3.1. Single MR bearing and MRA torque representation

To validate the reduced-order bearing-level representation, a single MR bearing was experimentally characterized before interpreting the planetary MRA behavior. The test used the same planetary gear and planet carrier from the MRA and was conducted under constant-velocity conditions at excitation currents of 0, 0.5, 1.0, and 1.5 A. This protocol isolates the dependence of bearing torque on speed and current.

Figure 4 shows the measured torque as a function of rotational speed. Under zero excitation current, the off-state torque remains low, decreasing from 0.0911 Nm at 0.5 rad s^{-1} to 0.0797 Nm at 5.0 rad s^{-1}. When current is applied, the torque increases substantially and exhibits a clear velocity-weakening trend: for 1.5 A, torque decreases from 1.1517 Nm at 0.5 rad s^{-1} to 0.5186 Nm at 5.0 rad s^{-1}, a reduction of 55.0%. This confirms that the activated MR bearing does not behave as a purely viscous damper and supports the assumptions of a phenomenological torque model.

The low-speed torque is dominated by the field-dependent pre-yield traction, governed by the apparent yield stress of the MR fluid and the bearing geometry. From the measured pre-yield values at $I = 0.5$, 1.0, and 1.5 A, the current-dependent pre-yield torque of a single MR bearing is represented by the empirical quadratic:

$$T_y(I) = 1.2126 - 1.2204I + 1.0952I^2, \tag{1}$$

which passes through the measured values $T_y = 0.8762$, 1.0874, and 1.8462 Nm, respectively. This quadratic is used as a local empirical map over the tested current range.

Beyond the pre-yield regime, torque decreases with increasing speed (post-yield) in a Stribeck-type velocity-weakening behavior. This is modeled phenomenologically as:

$$T_{\mathrm{MR}}(I,\omega) = T_y(I)\exp\left[-\left(\frac{|\omega|}{\omega_s}\right)^a\right], \tag{2}$$

where ω_s is the characteristic speed and a controls the shape of the velocity-dependent torque decay. Across the nonzero-current post-yield bearing data, this representation matches the measured torque with $R^2 \approx 0.94$, RMSE = 0.0486 Nm, and MAE = 0.0404 Nm.

For the full MRA, the pre-yield torque is better represented by a Hill-type saturation map, fitted from actuator-level measurements:

$$T_{y,\mathrm{MRA}}(I) = \frac{26.6 I^{2.88}}{0.5125^{2.88} + I^{2.88}}, \tag{3}$$

which captures the higher torque amplitude of the combined bearings and planetary transmission.

The corresponding post-yield MRA torque is represented as:

$$\begin{aligned} T_{\mathrm{MRA,post}}(I,\omega) &= T_{\mathrm{off,MRA}}(\omega) \\ &+ \beta_{\mathrm{MRA}}\, T_{y,\mathrm{MRA}}(I) \exp\left[-\left(\frac{|\omega|}{\omega_{s,\mathrm{MRA}}}\right)^{a_{\mathrm{MRA}}}\right], \end{aligned} \tag{4}$$

where the exponential term captures the velocity-weakening decay, and $\beta_{\mathrm{MRA}} = 0.5440$ is the empirical ratio that scales the MRA pre-yield torque capacity to its effective post-yield response after chain breakage and continuous shearing. The fitted speed-decay parameters are $\omega_{s,\mathrm{MRA}} = 2.15$ rad s^{-1} and $a_{\mathrm{MRA}} = 1.13$.

A simplified planetary torque-scaling calculation was used to approximate the actuator-level MRA torque from the measured single-bearing torque. The geometric parameters used for this calculation are the number of planet gears $N = 3$, the actuator output reduction ratio $G = 6.33$, the Sun gear tooth number $z_s = 9$, the planet gear tooth number $z_p = 19$, and the ring gear tooth number $z_r = 48$.

Since the Sun and planet gears have the same module, the pitch-radius ratio can be expressed as

$$\frac{R_s}{R_p} = \frac{z_s}{z_p} = \frac{9}{19}, \tag{5}$$

where R_s and R_p are the pitch radii of the Sun and planet gears, respectively.

For each planet gear, the tangential mesh force generated by the measured single-bearing torque T_b can be estimated as

$$F_t = \frac{T_b}{R_p}. \tag{6}$$

The corresponding Sun-side torque contribution is therefore $F_t R_s$. Considering the three planet gears and reflecting the torque to the actuator output side through the reduction ratio, the estimated output torque is

$$T_{\mathrm{out,est}} = G N T_b \frac{R_s}{R_p}. \tag{7}$$

At $I = 1.5$ A and $\omega = 0.5$ rad s^{-1}, the measured single-bearing torque is $T_b = 1.1517$ Nm. Substituting this value into equation (7) gives 10.35 Nm. The experimentally measured full-MRA torque under the same current and low-speed condition is 12.17 Nm, corresponding to a difference of approximately 14.9%. This indicates that the bearing-level torque, when transmitted through the planetary gear geometry and actuator output reduction, provides a reasonable estimate of the actuator-level torque scale. The small difference can be attributed to nonideal load sharing among the three planet gears, gear mesh losses, additional bearing friction, and differences between the isolated bearing test boundary condition and the fully assembled planetary MRA.

Although the single-bearing and full-MRA responses share the same Stribeck-type form, the full MRA torque cannot be obtained by directly multiplying the single-bearing torque by the number of bearings and the gear ratio. In the complete actuator, the torque is also affected by load sharing among the planet gears, transmission losses, and post-yield fluid shearing. Therefore, the MRA-level parameters in equation (4) are identified from actuator-level experiments and should be interpreted as an effective system-level representation of the fabricated prototype. Using this model, the fit metrics are strong ($R^2 = 0.9905$, RMSE = 0.288 Nm, MAE = 0.222 Nm), confirming that the single-bearing Stribeck structure is suitable for the full MRA trend, with adjusted amplitude and parameters reflecting the larger mechanical system. These experiments demonstrate that the phenomenological Stribeck-type torque model, derived from single-bearing data, captures the qualitative trends observed in both pre-yield and post-yield regimes and provides a reliable framework to interpret the torque behavior of the full MRA.

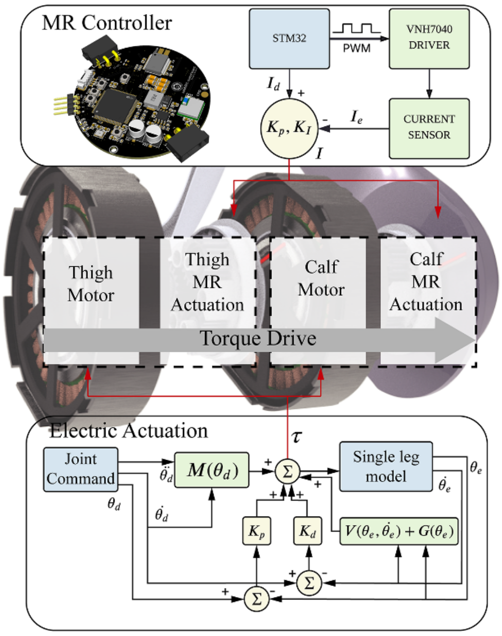

Figure 5. Control system of a single-legged robot with MR-Joints.

3.2. Control system integration

The single-legged robot employs MR-enabled joints at the thigh and calf, mounted in parallel with the leg linkage such that the electric actuator and MR bearing share the same torque transmission path (figure 5). This parallel configuration allows the resistive torque generated by the MR bearing to be directly superimposed on the electric actuator output, enabling seamless coordination between electric actuation and MR-based braking or damping.

The electric actuator operates in position control using a closed-loop Proportional–Derivative control strategy for accurate joint motion tracking. The motor torque command is given by

$$T_{\mathrm{motor}} = K_{\mathrm{p}} \left(\theta_{\mathrm{d}} - \theta_{\mathrm{e}}\right) + K_{\mathrm{d}} \left(\dot{\theta}_{\mathrm{d}} - \dot{\theta}_{\mathrm{e}}\right), \tag{8}$$

where T_{motor} is the torque generated by the electric actuator, KK_{p} and K_{d} are the position and velocity gains, θ_{d} and $\dot{\theta}_{\mathrm{d}}$ are the desired joint position and velocity, and θ_{e} and $\dot{\theta}_{\mathrm{e}}$ are the measured joint states.

To compensate for gravity and joint dynamics, a model-based dynamic compensation term is incorporated into the control loop, expressed as

$$T_{\mathrm{comp}} = M\left(\theta_{\mathrm{e}}\right) \ddot{\theta}_{\mathrm{e}} + V\left(\theta_{\mathrm{e}}, \dot{\theta}_{\mathrm{e}}\right) + G\left(\theta_{\mathrm{e}}\right), \tag{9}$$

where T_{comp} denotes the compensation torque, $M(\theta_{\mathrm{e}})$ is the joint-space mass matrix, $V(\theta_{\mathrm{e}}, \dot{\theta}_{\mathrm{e}})$ represents Coriolis and centrifugal effects, and $G(\theta_{\mathrm{e}})$ accounts for gravitational loading.

External contact forces acting at the foot are mapped to joint torques through the Jacobian transpose,

$$T_{\mathrm{contact}} = J\left(\theta_{\mathrm{e}}\right)^{\top} F_{\mathrm{e}}, \tag{10}$$

where T_{contact} is the vector of joint torques induced by external contact, $J(\theta_{\mathrm{e}})$ is the configuration-dependent Jacobian matrix evaluated at θ_{e}, and F_{e} is the external force vector applied at the end-effector.

In addition to electric actuation and contact-induced torques, the MR bearing introduces a resistive torque along the same actuator torque path. For control and system-level analysis, this resistance is represented by an equivalent MR torque T_{MR} acting at the joint level. Based on the pre-yield and post-yield mechanisms discussed previously, the MR torque is modeled as

$$T_{\mathrm{MR}}\left(I, \omega\right) = T_{\mathrm{off}} + T_{\mathrm{pre}}\left(I\right) + T_{\mathrm{post}}\left(I, \omega\right), \tag{11}$$

where T_{off} accounts for off-state drag, $T_{\mathrm{pre}}(I)$ captures the field-dependent pre-yield traction contribution, and $T_{\mathrm{post}}(I, \omega)$ represents the rate-dependent post-yield correction.

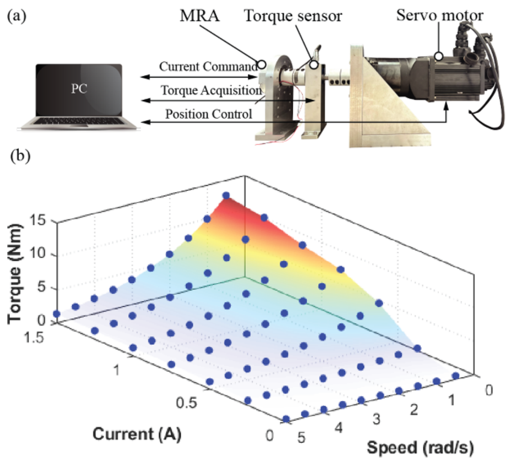

Figure 6. Experimental setup and post-yield damping torque characterization of the MRA: (a) Test rig layout (b) Steady-state torque versus current and rotational speed under continuous rotation.

The resulting joint torque command applied by the controller is given by

$$T = T_{\mathrm{motor}} + T_{\mathrm{contact}} + T_{\mathrm{MR}} + T_{\mathrm{comp}}. \tag{12}$$

The MR actuation is governed by a dedicated controller implemented on an STM32 microcontroller. The system employs VNH7040AY H-bridge drivers and an integrated current sensing circuit to regulate the excitation current supplied to the coils. Pulse-width modulation signals generated by the STM32 are used to control the coil current, enabling rapid magnetization and demagnetization of the MRF. A closed-loop PI current controller ensures accurate tracking of the desired excitation current.

Both the electric actuator controller and the MR current controller are integrated within the ROS framework. Serial communication between the ROS-based high-level controller and the STM32 enables synchronized commanding and real-time coordination between electric actuation and MR-based resistive torque modulation.

4. Actuator-level characterization and model identification

4.1. Post-yield damping torque evaluation

An experimental setup was constructed to evaluate the post-yield damping behavior of the proposed MRA under different excitation currents and rotational speeds. The setup consisted of a servo motor, a dynamic torque sensor, and an MR controller regulating the coil current supplied to the MRA, as illustrated in figure 6(a). The actuator was driven under continuous rotation while the excitation current was varied from 0 to 1.5 A in increments of 0.25 A. For each current level, experiments were repeated over a range of angular speeds from 0 to 5 rad s^{-1} with 0.5 rad s^{-1} increments. The resulting steady-state torque measurements are summarized in figure 6(b).

As shown in figure 6(b), the transmitted resistive torque exhibits a clear dependence on both excitation current and rotational speed. For a given current level, the resistive torque is higher at lower rotational speeds and decreases gradually as the speed increases. This speed-dependent reduction is most evident in the low-to-moderate speed range, after which the measured torque gradually approaches a plateau beyond approximately 4 rad s^{-1} over the tested current range. In the full MRA, the measured torque reflects the combined response of the MR bearings, planetary transmission, and off-state mechanical losses. Therefore, the experimentally observed speed-dependent trend is represented in this work using the reduced-order phenomenological velocity-weakening model in equation (4), rather than a first-principles description of the detailed fluid mechanics inside the bearing. This representation supports the use of an actuator-level rate-dependent resistive torque component for describing the post-yield damping behavior of the MRA.

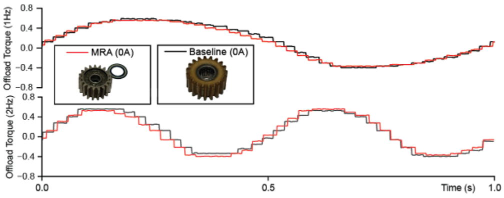

Figure 7. Off-state torque comparison between a conventional actuator and the MR-modified actuator under sinusoidal reciprocating rotational motion at 1 Hz and 2 Hz, corresponding to one and two motion cycles per second, respectively, with zero excitation current ($I = 0$ A).

4.2. Off-state torque offset

Considering the intended application of the MRA in a single-legged robotic joint, a sinusoidal position input was selected to approximate the cyclic angular motion of the joint and to evaluate the passive torque offset introduced by the MRF under zero excitation current. The MRA was compared with a conventional actuator under identical sinusoidal motion conditions with $I = 0$.

Figure 7 shows the measured torque responses at excitation frequencies of 1 Hz and 2 Hz, corresponding to one and two complete sinusoidal position cycles per second, respectively. In both cases, the MRA exhibits a resistive torque comparable to that of the conventional actuator. The replacement of the conventional needle bearing with a deep-groove ball bearing preserves motion smoothness, and with an appropriate MRF formulation the torque traces remain smooth and symmetric. No yield-like behavior is observed, confirming that the measured response arises purely from passive bearing and fluid effects. The off-state torque offset remains small relative to the field-activated torque levels reported in subsequent sections, indicating that the passive penalty introduced by MR integration is limited and does not significantly impede actuator backdrivability when unpowered.

This off-state characterization excludes degraded actuation performance under zero excitation current and establishes a baseline for a fair comparison between the MRA and the conventional actuator.

4.3. Pre-yield braking torque evaluation

To demonstrate the experimental effect of braking torque under different currents, we repeated the experiment with a constant speed of 0.1 rad s^{-1} of with an interval of 0.1 A from 0.1 to 1.5 A. The relationship between current and braking torque is shown in figure 8. The experiment data are extracted and repeated five times, and the average data are plotted. The braking torque increases along with the current and reaches a maximum braking torque of 26.15 Nm at a current of 1.5 A. Exceeding 1.5 A shows marginal torque enhancement due to the saturation of the MRF, indicating that further current input beyond this threshold does not significantly improve braking performance. This upper-current testing range was therefore used to experimentally determine the prototype's maximum braking capacity and saturation tendency, rather than to define the preferred near-linear control range identified from the magnetic-field simulation.

The trend of the braking torque can be curve-fitted using a Hill (sigmoid) function. The fitted hill function is as follows:

$$T(I) = \frac{T_{\max} I^n}{K^n + I^n} \tag{13}$$

yielding the parameter (table 2) estimates (mean ± SE): $K = 0.5127 \pm 0.0186$, $n = 2.8797 \pm 0.2708$, and $T_{\max} = 26.597 \pm 0.818$ N · m, based on $N = 15$ data points. The goodness-of-fit was high with coefficient of determination $R^2 = 0.9916$ (adjusted $R^2 = 0.9902$) and reduced chi-square $\chi^2_{\text{red}} = 0.817$.

To quantify prediction error, the mean absolute error (MAE) and root-mean-square error (RMSE) were computed across the dataset: MAE = 0.651 N · m and RMSE = 0.809 N · m. The maximum absolute deviation was 1.78 N · m at $I = 0.5$ A. Normalizing RMSE by the full observed torque range (0.60–26.15 N · m, range = 25.55 N · m) gives nRMSE = 3.16%, indicating that the fitted curve effectively captures the MR clutch output characteristics and enables precise control of the MRA output torque.

We fit the static current-torque relation with a Hill (sigmoid) function, which is algebraically a logistic in log-current. This is consistent with prior MR-damper works that employ sigmoid nonlinearities in their dynamic models [25, 26], though here we use the sigmoid only as a static capacity map rather than a full hysteresis model. The resulting static map closely aligns with prior reports of current-induced saturation in MR devices [27, 28].

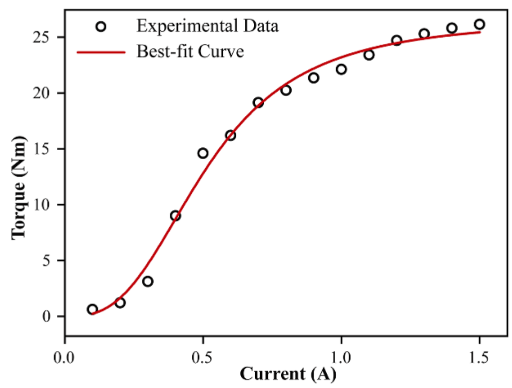

Figure 8. Results of MRA under braking effect. The input current varied from 0 to 1.5 A in steps of 0.1A, and the braking torque was recorded.

Table 2. Hill function fitting parameters.

Model	Hill Function
equation	$T_{\max} \cdot x^n/(K^n + x^n)$
Plot	Torque
K	0.51272 ± 0.01856
n	2.87967 ± 0.27077
$T_{\max}$	26.59697 ± 0.81828
Reduced Chi-Sq	0.81733
R-Square (COD)	0.99163
Adj. R-Square	0.99024

4.4. MR torque dynamics and response time

To characterize the transient response of the MRA, a step current input was applied while the actuator was rotated at a constant speed of 1.3 rad s^{-1}. The experimental setup consisted of a Unitree GO-M8010-6 motor supplying input torque, with the MRA and a torque sensor arranged in series (figure 9(a)). The test protocol was as follows: 0–2 s, the MRA was unpowered; 2–4 s, excitation current fixed at 1.5 A; and at 4 s, demagnetization was commanded to remove residual flux.

From 0 to 2 s, the measured off-state torque was approximately 0.7 N·m. At $t = 2.06$ s, the step current was applied. A command-to-current latency of approximately 44 ms was observed, after which the coil current reached 1.5 A within ∼21 ms under the PI-controlled loop. The torque followed the current increase closely (figure 9(c)), reflecting the combined effects of coil magnetization and MR fluid response.

The total system-level response time, defined from current application to torque plateau, was approximately 100 ms (t = 2.06–2.16 s). This interval includes the MR fluid's intrinsic viscoelastic response, the motor torque ramp, controller dynamics, and mechanical compliance. To assess the practical damping performance in the robotic system, the effective response time was also measured based on the actual deceleration of the motor. During the same step, the motor slowed from 1.3 rad s^{-1} at $t = 2.04$ s to 0 rad s^{-1} at $t \approx 2.10$ s, giving a system-level practical damping response time of 60 ms. This interval captures the time over which the MRA fully stops the actuator and represents the effective damping experienced during operation.

During the energized interval (2–4 s), both torque and displacement remained essentially constant, indicating that the MRA resisted the applied motor torque and operated in *braking mode*. After demagnetization at $t = 4$ s, the torque decayed smoothly to the off-state value over 4–6 s, returning to approximately 0.7 N·m, consistent with the pre-magnetization condition.

These results demonstrate that the MRA exhibits a rapid electrical and mechanical response. The measured system-level response time (100 ms) reflects the combined influence of motor dynamics and MR fluid behavior, while the practical damping interval (60 ms) represents the effective time over which the actuator is fully stopped by MR braking.

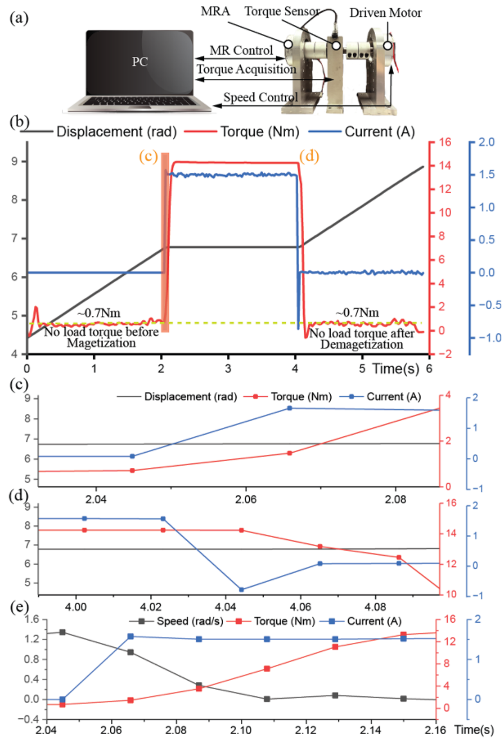

Figure 9. (a)Experiment setup with torque source as input (b)Intrinsic response time of MRA based on current tracking (c)Torque and current response during step input (2–4 (s) (d)Torque decay during demagnetization (4–6 (s) (e) System-level MRA damping response: motor speed decreases from 1.3 rad s^{-1} to 0 rad s^{-1} under MR braking, the 60 ms interval reflects the practical damping response time.

5. Single legged robot application

5.1. Impact loading evaluation

Leveraging the damping characteristics of the MRA, we evaluated a single robot leg on a one-degree-of-freedom (1-DOF) test stand, using the control architecture described in section III-D. Two operating modes were tested: (i) *Dual Actuation Mode*—both electric and MR actuation energized; and (ii) *Baseline Mode*—electric actuation only, with the MRA unpowered. Drop tests were performed by releasing the single-legged robot from prescribed heights while recording joint torques and vertical (Z-axis) accelerations during landing. In Dual Actuation Mode, the MRA was energized throughout the fall. Each experiment was repeated across multiple heights, with outcomes classified as *successful* if the robot landed without triggering the electric actuator's over-current protection, and *failure* if an over-current shutdown occurred (figure 10(a)).

To further evaluate robustness, actuator gains were tuned and the tests repeated (figure 10(b)). The results demonstrate that Dual Actuation Mode consistently enabled safe drops from heights increased by +5 cm compared to Baseline across all gain settings. The reduction of impact torque provided by the MRA afforded additional tolerance to landing loads, extending the allowable drop height while maintaining consistent performance. These results highlight the role of MR damping in improving landing reliability under high-impact conditions. At the maximum tested drop height of 65 cm, figure 10(c) reports the mean impact torque of both joints over five trials (error bars: ±1 SD). Relative to Baseline, Dual Actuation Mode reduced impact torque by 28%; this reduction was statistically significant (Welch's t-test, $p < 10^{-4}$, $n = 5$), confirming a wider safety margin during landing. Figure 10(d) shows the Z-axis acceleration *during impact*: with Dual Actuation Mode, the **peak impact acceleration** decreased from 62.14 ± 3.16 m s^{-2} (Baseline) to 54.97 ± 2.25 m s^{-2} (Dual Actuation), corresponding to an 11.5% reduction ($n = 5$). These findings demonstrate that during impact ($T_{ext} > T_{MR}$), the MRA provides a damping effect that complements electrical actuation, thereby reducing impact torques and increasing the safety margin for absorbing shocks from greater heights. Collectively, these results support Dual Actuation Mode as a safer and more reliable approach for high-impact operation in robotic applications.

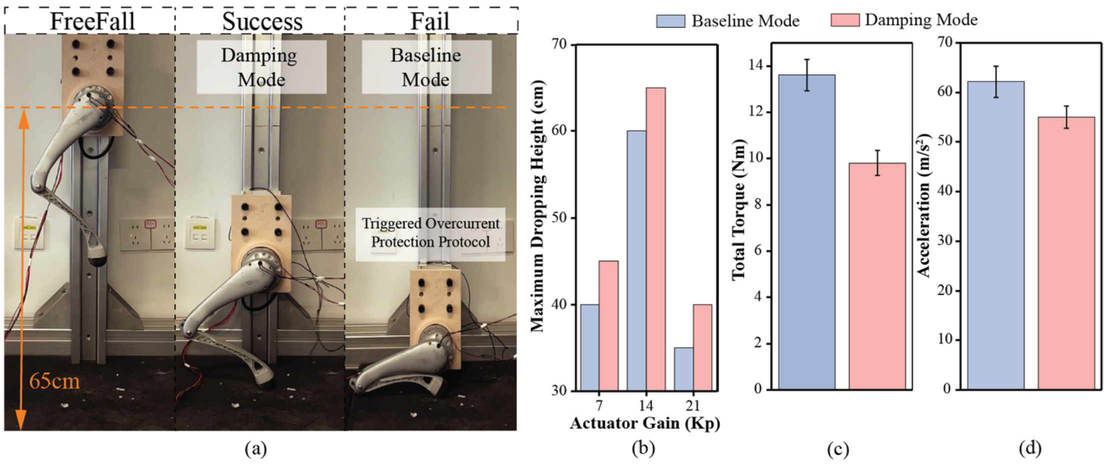

Figure 10. Impact Loading Evaluation. (a) Drop test from a height of 65 cm, with the experiment terminating when the actuator stops actuating due to overcurrent shutdown (b) Maximum drop height across different actuator gains for MR Damping Mode and Baseline Mode. (c) Total impact torques of single legged robot during impact (Error bars denote 1 SD) (d) Acceleration measurements of the single leg upon impact for both Modes.

5.2. Load capacity evaluation

To evaluate the effect of MRA with a single-legged robot on load capacity under dual actuation mode, we conducted a quasi-static loading test. The MRA are provided with 0.5 A to both of the MRA throughout the experiment. The payload was placed on top of the legged robot platform with an increment of 1 kg (figure 11(a)). The experiment concludes when the legged robot's joint reaches its stroke limit. Figure 11(b) compares the total electrical power consumption between dual actuation mode and Baseline Mode under different actuator gains(high/low). The power consumption under dual actuation included the coil excitation power (2.5 W per MRA) in addition to motor power for a fair comparison. When the MRAs are energized, the leg exhibited minimal compression due to the braking effect demonstrated by the MRA when ($T_{\text{ext}} < T_{\text{MR}}$. With the help of MRA, it sustained a payload of up to 9 kg with a total draw of 8.072 W. By contrast, the Baseline configurations supported only 2 kg at 11.62 W (low gain) and 6 kg at 22.80 W (high gain). Notably, with a constant 6 kg payload, the robot in dual actuation mode sustained 6kg at 7.136 W, which is 31.2% of the power consumption required by the Baseline (22.80 W) to support the same load. This demonstrates that MR actuation provides an efficient, controllable torque path for heavy-load support in legged robots.

6. Discussion

6.1. Results

The MR-Joint is designed to provide a dual-actuation system for robotic applications, enabling seamless switching between electrical actuation for precise position control, MR actuation for efficient torque density during load-bearing tasks, and parallel operation of both modes to achieve damping mitigation during impacts. Unlike conventional MR devices, which are often bulky and function solely as dampers, our design integrates the MR actuation system within the MR-Joint, minimizing added mass and volume. The custom-formulated MRF enhances fluidity and reduces friction within the MRA, ensuring that the performance of the electrical actuator is not compromised. In single-legged experiments, the dual-actuation configuration reduced impact torque by 28% and peak Z-axis acceleration by 11.5% compared to a purely electric baseline. These reductions confirm that the MRA effectively dissipates impact energy and protects the electric actuator from saturation and over-current faults-key limitations in high-impact robotic tasks. Quasi-static load tests further showed that the MRA-enabled joint sustained a 9 kg payload with only 8 W of power, highlighting enhanced load capacity, improved impact robustness, and reduced energy consumption. Collectively, these results demonstrate that MRA integration enhances both operational safety margins and efficiency during high-impact events.

6.2. Temperature effects and long-term durability

To evaluate the effect of sustained actuation on the MRA damping performance, a long-duration sinusoidal test was conducted at a 1 Hz position command for 1 h under an excitation current of 1 A. Over

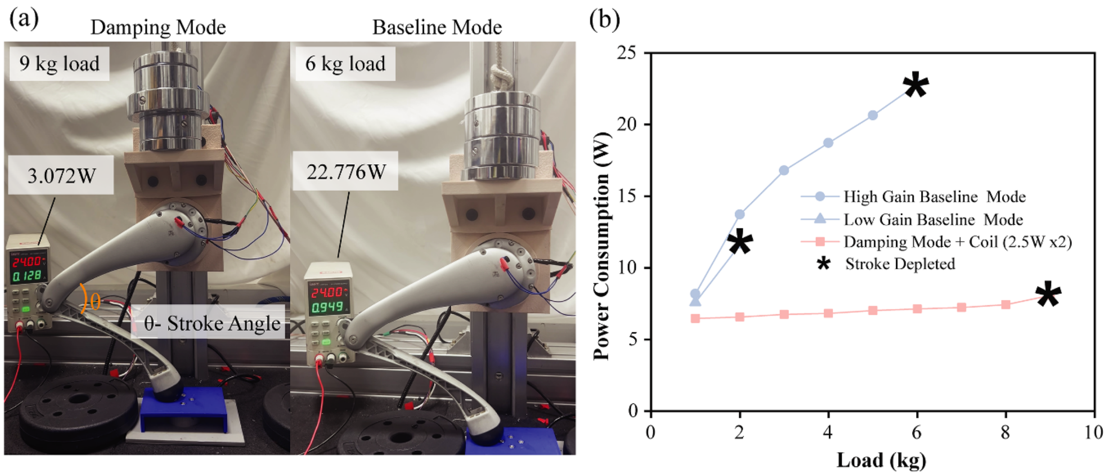

Figure 11. Load capacity evaluation. (a) Single-leg loading test, terminated when the stroke is completely depleted. (b) Power consumption of single leg under different loads, compared between the MR Actuation Mode and the High/Low Gain Baseline Modes.

the course of the test, the measured damping-torque amplitude decreased from 8.21 Nm to 6.165 Nm, corresponding to a 24.9% reduction while retaining approximately 75.1% of the initial damping capacity. This result demonstrates that long-duration cyclic operation reduces the available damping torque, likely due to a combination of viscous heating, temperature-dependent changes in MR fluid properties, and particle redistribution within the confined bearing volume.

To assess bearing durability under repeated actuation, a single MR bearing was installed in the original planetary assembly and driven by an external motor at 4 rad s^{-1} with 1 A excitation for 100 000 rotations. Initial measurements at 0.5 rad s^{-1} yielded an average activated damping torque of 0.75 Nm and an off-state torque of 0.08 Nm. After the endurance test and allowing the coil to cool, repeated measurements showed an average activated torque of 0.55 Nm, representing a 26.7% reduction, while the off-state torque remained essentially unchanged. These results indicate that the MR bearing retains smooth rotation when unpowered and continues to provide field-dependent damping, although with reduced peak torque.

Both the temperature- and wear-related reductions in damping torque highlight practical limitations of the current compact design. Future work will incorporate embedded temperature monitoring, extended cycling tests, direct inspection of particle distribution, and thermal-management strategies to quantitatively evaluate the influence of temperature and long-term operation on actuator performance.

6.3. Comparison of MR actuators

A key contribution of this work is the compact design of the proposed MRA, which achieves high torque density through the rheological properties of MRF while remaining lightweight and volume-efficient. To contextualize these advantages, a comparative analysis against representative MR-based actuators reported in the literature is conducted, with design-oriented characteristics summarized in table 3 while quantitative torque-density metrics, including TMR ratios and Torque-to-volume ratio (TVR) in the MR braking/load-holding regime are compared in table 4.

As shown in table 3, existing MR-based actuators differ primarily in how the electric actuation is integrated with the MR unit. Some designs embed the electric actuator directly within the MR device, forming a tightly coupled electromechanical unit [20]. Other approaches employ an external electric motor whose torque is transmitted to the MR unit via auxiliary belt or gear-based transmissions [21]. Alternatively, the electric motor may be mechanically connected in series with a standalone MR unit, where the MR device functions as a clutch or brake along the torque path [29, 30]. These architectural choices introduce trade-offs in system complexity, integration footprint, and achievable torque density.

Among these designs, the MR actuation joint reported in [20] represents the closest architectural comparison, as it integrates both electric and MR actuation within a single joint module. While that system achieves a TMR ratio of approximately 30 Nm kg^{-1} and a TVR ratio of 3.82×10^{-5} Nm mm^{-3},the proposed MRA, when evaluated in the MR braking/load-holding regime, achieves a TMR of 52.3 Nm kg^{-1} and a TVR of 8.4×10^{-5} Nm mm^{-3}. This corresponds to a 74.3% increase in TMR and an approximately 120% improvement in TVR for comparable torque capacity.

Table 3. Design-oriented comparison of MR-based actuators integrated with geared transmissions.

References	MR device type	MR placement	Actuation method
This work	MR bearing / damper	Planet gear support bearings (planetary stage, bearing-embedded)	Single electric actuator with embedded MR unit for semi-active damping and load support
Pisetskiy and Kermani [21]	Multi-disk MR clutch	Internal (MR clutch as the primary torque-transmission element inside the drivetrain)	Single actuation source driving joints via paired MR clutches for bidirectional torque transmission
Véronneau *et al* [20]	Single-disk MR clutch	Output stage (between dual motor chains and output gear)	Dual-motor, dual MR-clutch power chains combined at a single output
Pisetskiy and Kermani [30]	MR clutch (squeeze-mode)	Planetary gear meshing region (squeeze-mode interface)	Planetary clutch-based actuation exploiting gear-induced squeeze of MR fluid
Christie *et al* [29]	Single-disk MR brake / damper	Ring gear of planetary differential (internal DOF control)	Single motor driving Sun gear with MR-controlled differential transmission

Table 4. Torque density comparison of MR-based actuators.

Actuator	Type	Torque (Nm)	Mass (kg)	Volume (mm^3)	TMR ($Nm\,kg^{-1}$)	TVR ($Nm\,mm^{-3}$)
Our work (MR Joint)	Joint	26.15	0.50	3.11×10^5	52.3	8.40×10^{-5}
Our work (MRA)	Actuator	26.15	0.15	6.21×10^4	174.3	4.21×10^{-4}
Véronneau *et al* [20]	Joint	27.0	1.10	7.05×10^5	30.0	3.82×10^{-5}
Pisetskiy and Kermani [21]	Actuator	223.0	6.90	—	32.3	—
Ma *et al* [31]	Actuator	31.5	0.56	—	56.3	—
Plante *et al* [22]	Actuator	137.0	1.60	—	86.0	—

Note: In this table, 'Joint' refers to an integrated actuator module that includes the electric motor and MR element within a single joint-level unit, whereas 'Actuator' denotes a standalone MR device that requires an external electric motor and transmission to generate joint torque. For the proposed MR joint and MRA, the reported torque, TMR, and TVR values correspond to the MR braking/load-holding regime rather than continuous active motion or continuous actuation.

When compared with MR actuators that do not incorporate an embedded electric drive, the proposed MRA further demonstrates a substantially higher torque density, achieving a TMR of 174.3 $Nm\,kg^{-1}$ and exceeding the reported values of many alternative designs listed in table 4. The resulting reduction in actuator mass and volume directly translates to lower joint inertia, which is particularly advantageous for legged robotic applications where dynamic efficiency and impact robustness are critical.

In addition, the MR planetary-based design enables seamless integration with mainstream robotic actuation architectures that already employ planetary transmissions, such as those used in the MIT Cheetah, Unitree Go1, Go2, and B1 platforms. The proposed MRA therefore achieves a favorable balance between torque output, compactness, and integration compatibility, providing a practical alternative actuation solution for robotic systems requiring both high torque density and adaptive damping capability.

6.4. Broader implications

The demonstrated impact mitigation and load-support behavior of the proposed MRA makes it particularly well suited for quasi-static postures, landing phases, and load-bearing tasks, where conventional electric actuators typically consume significant energy to maintain position. By providing field-tunable resistive torque at the joint level, this approach supports the design of robotic systems that prioritize robustness, energy efficiency, and mechanical resilience across a wide range of applications, including legged locomotion, robotics manipulation, and wearable robotics.

7. Conclusion

In this paper, we presented a compact MR planetary actuator that embeds MR functionality directly within the planetary gear stage, enabling MR-based torque modulation in conventional actuators without requiring substantial mechanical redesign or changes to joint layout. This architecture is well suited for retrofitting existing robotic platforms with minimal modification. By exploiting the rheological properties of MRF, the proposed MRA demonstrates enhanced impact mitigation, improved load-support capability, and increased energy efficiency.

The proposed MRA demonstrates exceptional torque-density performance, achieving a TMR ratio of 174.3 $\mathrm{Nm\,kg^{-1}}$ and a TVR ratio of 4.21×10^{-4} $\mathrm{Nm\,mm^{-3}}$ at the actuator level. When evaluated at the joint level, the system maintains a high TMR of 52.3 $\mathrm{Nm\,kg^{-1}}$ and a TVR of 8.4×10^{-5} $\mathrm{Nm\,mm^{-3}}$. These metrics highlight the MRA's superior efficiency, indicating it can deliver high torque output while maintaining a compact form factor. These features make the MRA an ideal candidate for integration into high-performance robotic systems where both efficiency and compactness are critical.

Experimental validation on a single leg of a quadruped robot showed a 28% reduction in impact torque and an 11.5% reduction in peak Z-axis acceleration during drop tests, along with sustained support of a 9 kg payload at only 8 W in quasi-static loading. These results confirm that the MRA not only enhances resilience to high-impact events but also improves energy efficiency and load capacity, making it highly suitable for robotics applications where compactness and robustness are critical.

Acknowledgments

This work was supported by National Natural Science Foundation of China (Grant Nos. U21A20119, 52105081 and 62303002), State Key Laboratory of Micro-Spacecraft Rapid Design and Intelligent Cluster (Grant No. MS01240110), Major Project of Anhui Province's Science and Technology Innovation Breakthrough Plan (202423h08050003), Anhui's Key R&D Program of China (Grant No. 202104a05020009), USTC start-up funding (Grant No. KY2090000067), Key Program of Natural Science Foundation of Anhui Higher Education Institutions of China under grant (Grant No. 2022AH050068) and the Fundamental Research Funds for the Central Universities (SC5290005162).

Data availability statement

No new data were created or analysed in this study.

Conflict of interest

None of the authors has a conflict of interest to disclose.

ORCID iDs

Erwin Ang Tien Yew 0009-0005-4139-3140
Wenbo Li 0009-0001-7945-4958
Xianlong Mai 0000-0001-8273-5112
Shuaishuai Sun 0000-0002-8695-9217

References

[1] Hongjun M and Danyu R 2024 *Adv. Mech. Eng.* **16** 16878132241307827
[2] Kim Y, Lee Y and Cha Y 2021 *IEEE Access* **9** 41010–8
[3] Meng H, Zhang S, Zhang W and Ren Y 2024 *Sci. Rep.* **14** 25946
[4] Semini C, Tsagarakis N G, Guglielmino E, Focchi M, Cannella F and Caldwell D G 2011 *Proc. Inst. Mech. Eng. I* **225** 831–49
[5] Semini C, Barasuol V, Goldsmith J, Frigerio M, Focchi M, Gao Y and Caldwell D G 2016 *IEEE/ASME Trans. Mechatronics* **22** 635–46
[6] Semini C, Tsagarakis N G, Vanderborght B, Yang Y and Caldwell D G 2008 Hyq-hydraulically actuated quadruped robot: Hopping leg prototype *2008 2nd IEEE RAS & EMBS Int. Conf. on Biomedical Robotics and Biomechatronics* (IEEE) pp 593–9
[7] Khan H, Kitano S, Frigerio M, Camurri M, Barasuol V, Featherstone R, Caldwell D G and Semini C 2015 Development of the lightweight hydraulic quadruped robot-minihyq *2015 IEEE International Conf. on Technologies for Practical Robot Applications (TePRA)* (IEEE) pp 1–6
[8] Zhao P, Xie A, Zhu S and Kong L 2023 *Sci. Rep.* **13** 60
[9] Bledt G, Powell M J, Katz B, Di Carlo J, Wensing P M and Kim S 2018 Mit cheetah 3: Design and control of a robust, dynamic quadruped robot *2018 IEEE/RSJ Int. Conf. on Intelligent Robots and Systems (IROS)* (IEEE) pp 2245–52
[10] Boston Dynamics Spot (available at: https://bostondynamics.com/products/spot/) (Accessed 21 April 2025)
[11] Unitree Robotics Go1 (available at: www.unitree.com/cn/go1) (Accessed 21 April 2025)
[12] Zancewicz G and Hoefken C 2020 Impact of actuator torque density on expected robot life-a dynamic model *2020 5th Int. Conf. on Control and Robotics Engineering (ICCRE)* (IEEE) pp 30–36
[13] Chen M, Zhang B, Li H, Gao X, Wang J and Zhang J 2024 *Sensors* **24** 3747
[14] Puma-Benavides D S, Mixquititla-Casbis L, Llanes-Cedeño E A and Jima-Matailo J C 2024 *World Electr. Veh. J.* **15** 282
[15] Bilgin O and Kazan F A 2016 The effect of magnet temperature on speed, current and torque in pmsms *2016 XXII Int. Conf. on Electrical Machines (ICEM)* (IEEE) pp 2080–5
[16] Hsieh T H, Yeon S H and Herr H 2023 Energy efficiency and performance evaluation of an exterior-rotor brushless dc motor and drive system across the full operating range *Actuators* **12** 318
[17] Ashtiani M, Hashemabadi S and Ghaffari A 2015 *J. Magn. Magn. Mater.* **374** 716–30
[18] Moghani M and Kermani M R 2019 *IEEE/ASME Trans. Mechatronics* **25** 76–83
[19] Yadmellat P and Kermani M R 2013 Adaptive hysteresis compensation for a magneto-rheological robot actuator *2013 IEEE/RSJ Int. Conf. on Intelligent Robots and Systems* (IEEE) pp 4900–5
[20] Véronneau C, Denis J, Lhommeau P, St-Jean A, Girard A, Plante J S and Bigué J P L 2022 *IEEE Robot. Autom. Lett.* **8** 896–903
[21] Pisetskiy S and Kermani M 2021 *J. Intell. Mater. Syst. Struct.* **32** 2582–600
[22] Plante J S, St-Jean A and Lucking Bigué J P 2025 *Sci. Rep.* **15** 14363
[23] Song J, Zhu A, Tu Y, Zheng C and Cao G 2023 *IEEE Trans. Neural Syst. Rehabil. Eng.* **32** 43–52
[24] Song Z, Zhang W, Chen D, Ju W, Kang R and Dai J S 2024 *IEEE/ASME Trans. Mechatronics* **30** 2316–26
[25] da Silva D M D, Avila S M, de Morais M V G and Cavallini J A A 2024 *J. Braz. Soc. Mech. Sci. Eng.* **46** 134
[26] Zhang X, Zhang X, Zhao Y, Zhao J and Xu Z 2017 *Eng. Struct.* **132** 576–85
[27] Wellborn P S, Mitchell J E, Pieper N J and Webster R J 2021 *IEEE/ASME Trans. Mechatronics* **27** 3099–109
[28] Hu G, Wu L and Li L 2021 Torque characteristics analysis of a magnetorheological brake with double brake disc *Actuators* **10** 23
[29] Christie M, Sun S, Quenzer-Hohmuth J, Deng L, Du H and Li W 2021 *Smart Mater. Struct.* **30** 045013
[30] Pisetskiy S and Kermani M R 2020 A concept of a miniaturized mr clutch utilizing mr fluid in squeeze mode *2020 IEEE/RSJ Int. Conf. on Intelligent Robots and Systems (IROS)* (IEEE) pp 6347–52
[31] Ma H, Chen B, Qin L and Liao W H 2017 *Smart Mater. Struct.* **26** 035013